

Experimental and numerical investigation of the competition between axisymmetric time-periodic modes in an enclosed swirling flow

J. M. Lopez

Department of Mathematics and Statistics, Arizona State University, Tempe, Arizona 85287

Y. D. Cui

Temasek Laboratories, National University of Singapore, 119260 Singapore

T. T. Lim

Department of Mechanical Engineering, National University of Singapore, 119260 Singapore

(Received 29 June 2006; accepted 20 September 2006; published online 17 October 2006)

Time-periodic vortex flows in an enclosed circular cylinder driven by the rotation of one endwall are investigated experimentally and numerically. This work is motivated partly by the linear stability analysis of Gelfgat *et al.* [*J. Fluid Mech.* **438**, 363 (2001)], which showed the existence of an axisymmetric double Hopf bifurcation, and the purpose of the experiment is to see if the nonlinear dynamics associated with this double Hopf bifurcation can be captured under laboratory conditions. A glycerin/water mixture was used in a cylinder with variable height-to-radius ratios between $\Gamma=1.67$ and 1.81, and Reynolds numbers between $Re=2600$ and 2800 (i.e., in the neighborhood of the double Hopf). Hot-film measurements provide, for the first time, experimental evidence of the existence of an axisymmetric double Hopf bifurcation, involving the competition between two stable coexisting axisymmetric limit cycles with periods (nondimensionalized by the rotation rate of the endwall) of approximately 31 and 22. The dynamics is also captured in our nonlinear computations, which clearly identify the double Hopf bifurcation as “type I simple,” with the characteristic signatures that the two Hopf bifurcations are supercritical and that there is a wedge-shaped region in (Γ, Re) parameter space where both limit cycles are stable, delimited by Neimark-Sacker bifurcation curves. © 2006 American Institute of Physics.

[DOI: [10.1063/1.2362782](https://doi.org/10.1063/1.2362782)]

I. INTRODUCTION

The flow in an enclosed stationary circular cylinder driven by the constant rotation of one endwall is investigated both experimentally and numerically. This flow has attracted much attention due to the manner in which the angular momentum introduced into the system by the endwall rotation is redistributed to form a vortical flow about the axis, which consists of steady axisymmetric vortex breakdown recirculation zones.¹ There have been several axisymmetric numerical studies for cylinders with height-to-radius aspect ratios $\Gamma=H/R \in (1.6, 2.8)$,^{2–6} where H and R are the height and radius of the cylinder. A close examination of the linear stability results of Ref. 7 shows that in this aspect ratio range, where the steady basic state loses stability to axisymmetric time-periodic flow, there are two distinct Hopf bifurcations involved leading to axisymmetric states with different frequencies. The crossover point between these two Hopf bifurcations (the double Hopf bifurcation point) is at $\Gamma \approx 1.72$ and $Re = \Omega R^2 / \nu \approx 2665$ (see Fig. 1 of Ref. 7), where Ω is the rotation speed of the endwall and ν is the kinematic viscosity. As far as we are aware, no corresponding experimental study has been conducted in the neighborhood of this double Hopf point, and the desire to see if the nonlinear dynamics associated with this axisymmetric double Hopf bifurcation can be captured experimentally motivated the

present study. Nonlinear computations are also presented to provide a theoretical basis from which to interpret the experimental data.

II. EXPERIMENTAL APPARATUS AND TECHNIQUE

The apparatus used in the present investigation is shown schematically in Fig. 1. It is inverted from the actual experimental setup for ease of comparison with the experimental results of others that have the rotating disk at the bottom of the cylinder (flow visualization photos are also inverted). The description here is based on the figure as displayed.

The apparatus consists of a Plexiglas cylinder, with a matching rotating disk at the bottom and a stationary disk at the top of the cylinder. For convenience, commercial Plexiglas cylinders were initially used, but after several months of experimentation, it was discovered that slight variations in the radius of the cylinders led to significant changes in the results. Hence, we fabricated a new cylinder from a solid piece of Plexiglas rod and painstakingly polished it to optical quality to facilitate flow visualization. The resulting cylinder has an inner radius $R=8.625 \pm 0.005$ cm and a wall thickness of 2.1 cm. The rotating disk sits neatly on a high-precision thrust bearing mounted on an adjacent fixed plate, which in turn is push-fitted into the bottom end of the cylinder to ensure accurate alignment. The edge of the rotating disk has a maximum excursion of 0.040 mm (about 0.03°) and a

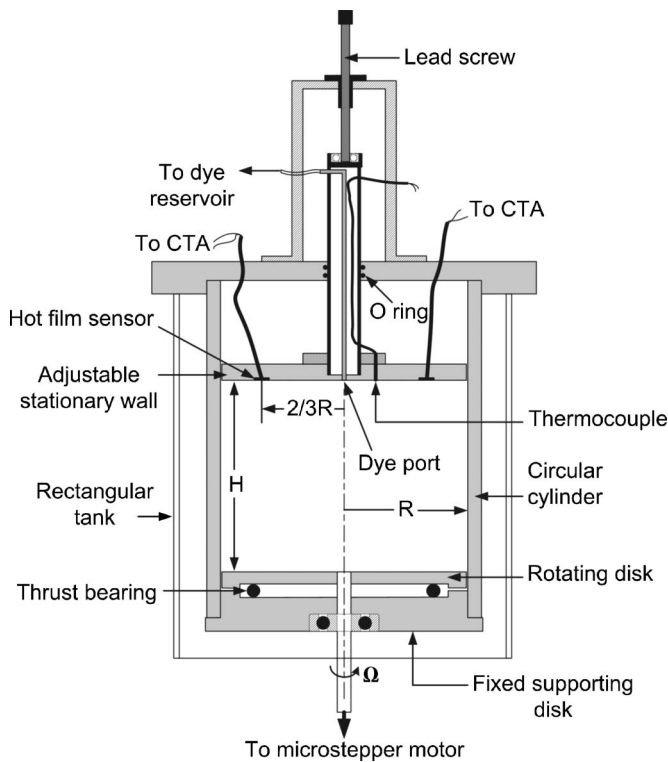


FIG. 1. Schematic of the flow apparatus.

nominal gap of 0.40 mm between the rotating plate and the cylinder. The disk was driven by a microstepper motor operating at 20 000 steps/rev, with an adjustable speed range of up to 240 rpm ($\Omega=25.1$ rad/s), controlled by a function generator with an accuracy of 0.1%. The knob of the function generator was specially modified with a worm-gear system so that the Reynolds number can be fine-tuned by as small as 1 at each step. The height H of the flow domain can be varied infinitesimally by changing the position of the stationary top disk using a 1 mm pitch screw stud to give a variable aspect ratio, $\Gamma=H/R$. In the present investigation, Γ was varied between 1.67 and 2.5 with an accuracy of 0.005. This unique feature of the apparatus allows incremental changes in Γ for a fixed Reynolds number, or vice versa.

The working fluid was a mixture of glycerin and water (roughly 75% glycerin by weight) with kinematic viscosity $\nu=0.404\pm 0.002$ cm²/s at a room temperature of 23.0°C. In all cases, the viscosity was measured using a Hakke Rheometer to an accuracy of about 0.5%, and the temperature of the mixture was monitored regularly using a thermocouple located at the bottom of the cylinder to the accuracy of 0.05°C, giving an uncertainty in the Reynolds number of about ± 10 in absolute value. To minimize flow image distortion due to the curvature of the cylinder, the whole cylinder was immersed in a rectangular Plexiglas box filled with the same working fluid (both the solution and the Plexiglas have similar refractive indices). Due to the length of time required to run each experiment, complicated by the fact that the cylinder wall is too thick to allow efficient heat exchange between the fluid inside the cylinder and its surroundings, there is a gradual increase in the temperature of the fluid, resulting in an increase in Re at a rate $\partial Re/\partial t \approx 25$ per hour. For ex-

periments with fixed Γ and varying Re , this issue was addressed by taking note of the temperature at the time the data were collected, and the Reynolds number was then recalculated based on the relationship between viscosity and temperature obtained using a Hakke Rheometer. The data were sampled and acquired over a short time interval (about 1 min) during which Re is nominally constant. For experiments with fixed Re and variable Γ , the rotation rate of the bottom disk was readjusted to account for the temperature rise in order to maintain Re constant.

Various techniques were tried to measure the oscillatory behavior of the flow, including particle image velocimetry (PIV), dye visualization, and glue-on hot-film. While PIV is an excellent technique to measure the overall flow field, it is not well suited to measure oscillatory flow behavior as it relies on capturing flow images discretely. Although both dye visualization and hot-film can provide good measures of the oscillatory flow behavior, hot-film was chosen as it has an added advantage, particularly in the vicinity of Hopf and Neimark-Sacker bifurcation curves, where the flow exhibits long transients during which dye diffusion limits visualization-based techniques. Two flush-mounting hot-films (Dantec 55 R47) were attached to the surface of the stationary end plate with water-proof glue. The nominal thickness of the sensor is less 0.1 mm, and therefore its effect on the flow was negligible. These two sensors were located at $2/3$ of the radius of the cylinder and 180° apart. It should be noted that the hot-films were not calibrated, primarily due to the design of the glue-on hot-film, which makes calibration against a known flow velocity difficult; once the hot-film is glued to a surface, it cannot be easily removed (without damage) for calibration in another facility. This is in contrast to the more conventional hot-film probe, which can be readily shifted between facilities for calibration, but of course such probes are significantly more intrusive than the glue-on hot-films. Nevertheless, calibration is not an issue for concern when measuring the temporal frequencies in a flow. Given that the frequencies of interest in the present investigation are below 1 Hz, the output signal of the hot-film from the constant temperature anemometer (CTA; Dantec 55 M01) was conditioned by a low-pass filter with a cutoff frequency of 10 Hz to eliminate high-frequency noise before it was amplified with an analog amplifier. The output signal was sampled at 100 Hz using a computer for subsequent analysis. Although laser Doppler anemometry (LDA) was not attempted in the present study due to the equipment not being available in our laboratory, past studies have shown that hot-film or hot-wire anemometry is as good as or even better than LDA when measuring oscillatory behavior for long times.

To capture flow images, food dye premixed with the working solution at low concentration was released very slowly into the flow domain through a 1.5 mm diameter hole at the center of the stationary top disk, and the flow images were recorded using a CCD camera at a rate of 25 frames per second for subsequent reproduction.

While the utmost care was taken to machine the cylinder to a high degree of accuracy and to set up the apparatus so that the flow would be axisymmetric, like all experiments,

the apparatus can never be 100% perfect and small unavoidable imperfections exist. To check the symmetry of the apparatus, experiments were conducted for the basic steady state at $Re=1853$ and $\Gamma=1.75$. This particular flow condition was chosen because it has a notorious history stemming from the experimental results of Ref. 8, in which it was reported that the flow at this point in parameter space was not axisymmetric. Linear stability analysis,⁷ however, showed theoretically that the steady axisymmetric state is stable to general three-dimensional unsteady perturbations, and numerous direct numerical simulations using the three-dimensional unsteady Navier-Stokes equations with small random perturbations in the initial conditions also show evolution to the steady axisymmetric basic state. Subsequent experiments at this point in parameter space have also been conducted⁹ and have shown that the degree to which the observed flow is three-dimensional can be reduced by reducing the level of imperfection in the apparatus. They obtained flow visualization results very similar to those of Ref. 8 by tilting the stationary endwall approximately 0.4° from horizontal (see their Fig. 3). The same flow has also been investigated numerically¹⁰ and computed streaklines in very close agreement with the dye visualization⁸ were obtained by numerically imposing a small misalignment of the rotating endwall (misalignment angle of about 0.1°). They also redid the linear stability analysis⁷ of the basic state using a different numerical method and reached the same conclusion: the axisymmetric state is stable to all three-dimensional perturbations at $\Gamma=1.75$ for $Re < 2800$ and unsteady axisymmetric flow appears at about $Re=2650$. It would thus seem that the three-dimensional nature of the flow visualization at low $Re=1850$ is not intrinsic to the flow but is due to extrinsic imperfections.

That the flow visualizations at $Re=1850$ are extremely sensitive to small imperfections is not surprising. The basic state has stagnation points on the axis; in the language of dynamical systems, these hyperbolic fixed points are structurally unstable,¹¹ and as pointed out in Ref. 12, "...certain degenerate invariant manifolds of homoclinic or heteroclinic orbits connecting the stagnation points can be expected to break up under arbitrary small perturbations." The question, of course, is whether these arbitrarily small imperfections have any effect on the dynamics of the flow.

Our experiments using commercial cylinders and the specially fabricated cylinder reported here suggest that if the imperfections are not too large, then they do not qualitatively alter the dynamics. We have made every effort to reduce the level of imperfections in the apparatus, but of course no apparatus is perfect. Figure 2 shows flow visualizations of the vortex breakdown bubble region at $\Gamma=1.75$ and $Re=1853$, using both fluorescent dye illuminated by a laser sheet and food dye with ambient lighting. The level of imperfection is apparently lower than in the experiments of Ref. 8 and somewhere in between the "perfect" and the 0.4° tilted cases of Ref. 9, although the causes of the imperfections in the various apparatus are probably different. The role of density differences between the dye and working fluid has also been considered.¹³ Note that the pictures in Fig. 2 have been reversed from the original blue dye with white background in

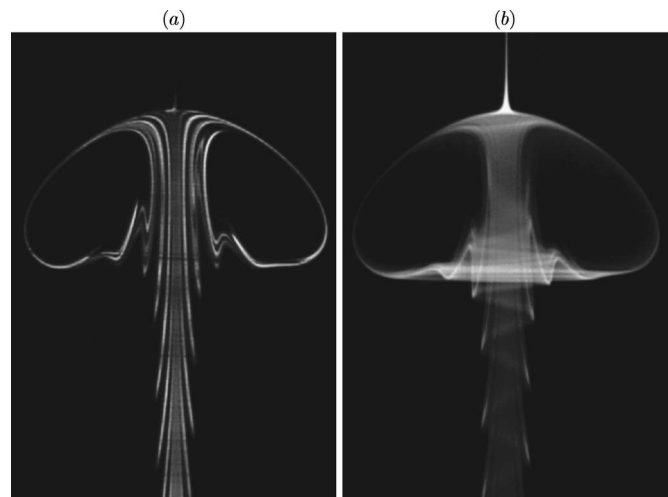


FIG. 2. Flow visualization at $Re=1853$, $\Gamma=1.75$, using (a) fluorescent dye illuminated by a laser sheet and (b) food dye with ambient lighting.

order to improve their contrast. The dye sheet seen in the figure is steady, it does not precess, and there is a clear $m=1$ azimuthal wave number associated with it. That being said, it must be remembered that although the dye port is located at the center of the stationary endwall, there is no certainty that the dye will emerge axisymmetrically about the axis $r=0$, and so even in a perfectly axisymmetric flow, a dye sheet that is released an arbitrarily small distance off-axis will have a nonaxisymmetric appearance with a predominately $m=1$ azimuthal wave number.^{4,14}

Based on our flow visualization results, which compare favorably with the result of Ref. 9, we decided to proceed with the hot-film measurements. Note that in our earlier experiments using commercial Plexiglas cylinders, distortions in those cylinders caused flow images like those presented in Fig. 2 to be highly nonaxisymmetric.

Before presenting the experimental results in the neighborhood of the double Hopf bifurcation, we next briefly describe the nonlinear numerical computations and spatio-temporal characteristics of the solutions, which are difficult to obtain completely from experiments.

III. NUMERICAL TECHNIQUE

The numerical simulations of this problem were performed using the spectral code described in Ref. 15 and previously used to explore the nonlinear dynamics of confined vortex breakdown flows.^{16–18} The results presented here have 48 Legendre modes in the radial and axial directions, and up to $N_\theta=16$ (resolving up to azimuthal wave number $m=16$; these were used to test the stability of the axisymmetric solutions to three-dimensional perturbations); the time step used is $\delta t=5 \times 10^{-3}$ (which is much smaller than needed for stability of the code in the parameter regime investigated).

IV. OVERVIEW OF THE NONLINEAR DYNAMICS

Over the parameter range reported here ($\Gamma \in [1.64, 1.80]$ and $Re \leq 2800$), we have found that the basic steady state bifurcates to axisymmetric limit cycle solutions

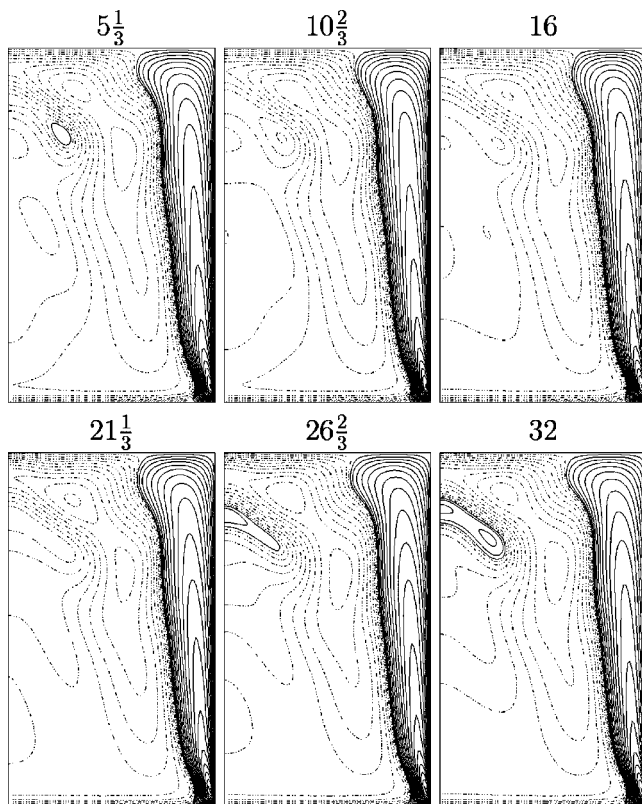


FIG. 3. Contours of w for the axisymmetric time-periodic state LC_1 at $Re=2700$, $\Gamma=1.72$ at six phases over one oscillation period ($T \approx 31.89$); there are 20 positive and 20 negative contours quadratically spaced, i.e., contour levels are $\pm 0.15(i/20)^2$ with $i=1 \rightarrow 20$. The solid (broken) contours are positive (negative). The left boundary is the axis and the bottom is the rotating endwall.

LC_1 and LC_2 with different frequencies, and that these are nonlinearly stable to three-dimensional perturbations. For several cases throughout the parameter regime in question, we have solved the three-dimensional governing equations resolving up to the $m=16$ azimuthal wave number, using the axisymmetric solution together with small random perturbations in all $m \neq 0$ modes as initial conditions. In all cases, the $m \neq 0$ components of the flow decay toward machine zero. At larger Reynolds numbers ($Re > 3000$), some $m \neq 0$ modes do grow and nonaxisymmetric solutions become stable.¹⁸

Near onset, the spatial characteristics of LC_1 and LC_2 are very similar to those of the steady state from which they bifurcate. For both limit cycles, the oscillations consist of pulsations in the vortex breakdown region. Figures 3 and 4 show contours of the axial component of velocity w for LC_1 and LC_2 , respectively, both at $Re=2700$ and $\Gamma=1.72$. As is clear from these figures, a snapshot of the flow structure at a point in time is not sufficient to distinguish between the two modes. Their only robust distinguishing characteristic is their period of oscillation, which is essentially independent of Re and varies linearly with Γ .

Figure 5 shows how the experimentally measured periods T (nondimensionalized with the rotation rate Ω rad/s) of LC_1 and LC_2 vary with Re for various Γ . The small variability ($<1\%$ over a considerable range of Re) in the oscillation period near onset is typical for a Hopf bifurcation. Figure 6

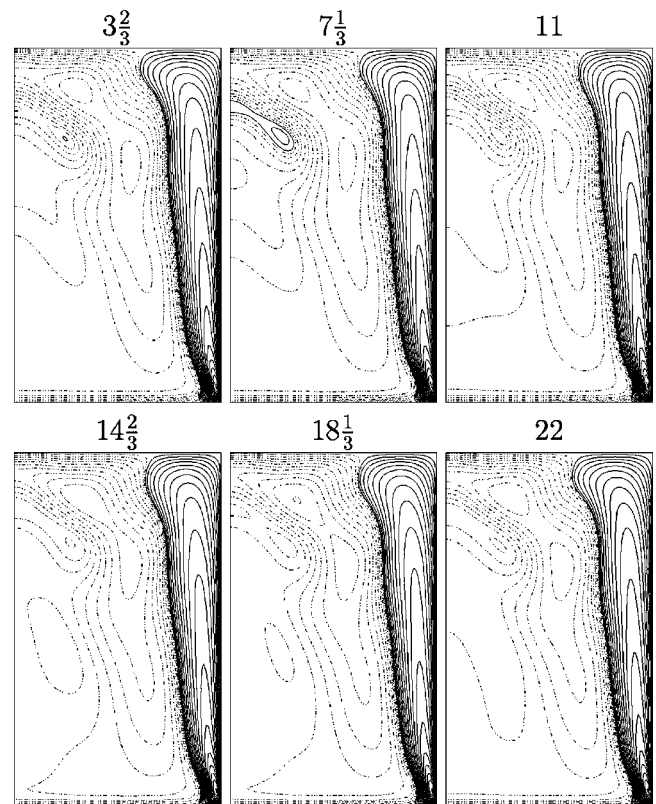


FIG. 4. Contours of w for the axisymmetric time-periodic state LC_2 at $Re=2700$, $\Gamma=1.72$ at six phases over one oscillation period ($T \approx 22.01$); there are 20 positive and 20 negative contours quadratically spaced, i.e., contour levels are $\pm 0.15(i/20)^2$ with $i=1 \rightarrow 20$. The solid (broken) contours are positive (negative). The left boundary is the axis and the bottom is the rotating endwall.

displays the variation with Γ of the nondimensional period averaged over Re , $\langle T \rangle$, for both LC_1 and LC_2 determined from hot-film measurements (open symbols) as well as from our nonlinear computations (filled symbols). The agreement between the experimentally and numerically determined periods is excellent, confirming that the unsteady experimental flow is axisymmetric. To further verify this, we present in Fig. 7 time series from the two hot-films placed 180° apart on the stationary end plate. Figure 7(a) is the output for an LC_1 state at $Re=2760$ and $\Gamma=1.704$, and Fig. 7(b) is for an LC_2 state at $Re=2750$ and $\Gamma=1.780$ (each state is asymptotically stable, and reached from different initial conditions). Notice that in both cases, the hot-film outputs are synchronized (peaks match in time), providing further experimental evidence of the axisymmetric nature of the limit cycles LC_1 and LC_2 .

The various observed states were obtained experimentally either by impulsively rotating the bottom disk to a desired Re with the fluid initially at rest, or by gradually varying either H or Ω to reach the desired point in parameter space while maintaining a particular flow state. Near bifurcation curves, the associated transients using either approach are extremely long. Following these approaches, the results obtained from the hot-film measurements are summarized in a state diagram Fig. 8, along with the numerically determined Hopf bifurcation curves H_1 and H_2 , whereupon cross-

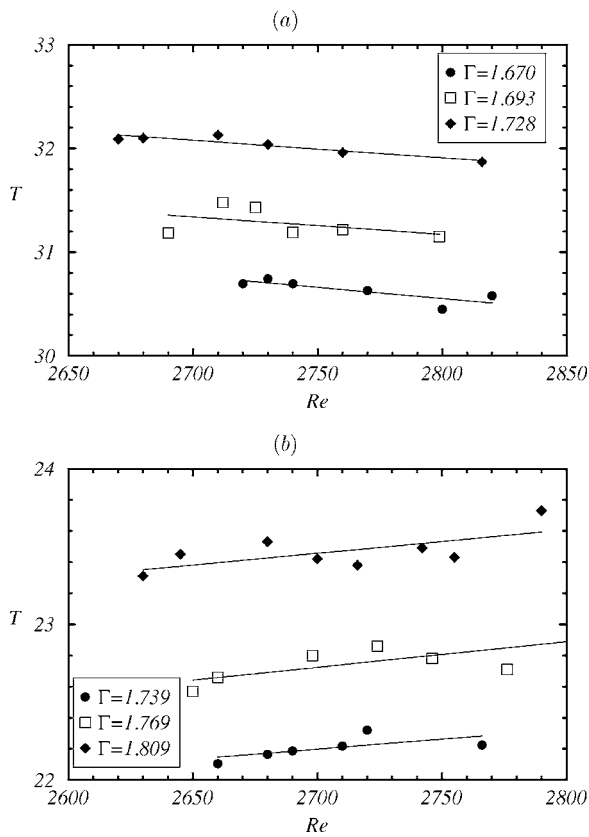


FIG. 5. Variation with Re of the experimentally measured oscillation period T (nondimensionalized with the rotation rate Ω rad/s) of (a) LC_1 and (b) LC_2 , for Γ as indicated.

ing these curves, LC_1 and LC_2 bifurcate from the steady basic state, respectively, and the numerically determined Neimark-Sacker curves NS_1 and NS_2 , whereupon crossing these LC_1 and LC_2 , respectively, change their stability, but continue to exist on either side of the curves. The double Hopf point at $\Gamma_{dH} \approx 1.723$ and $Re_{dH} \approx 2661$ is where these four curves meet. For the two Hopf bifurcation curves, we only show H_1 for $\Gamma \leq \Gamma_{dH}$ and H_2 for $\Gamma \geq \Gamma_{dH}$. These were determined numerically by extrapolating in Re the amplitude of the oscillations of the limit cycles LC_1 and LC_2 to zero at various fixed values of Γ . For the other halves of the two

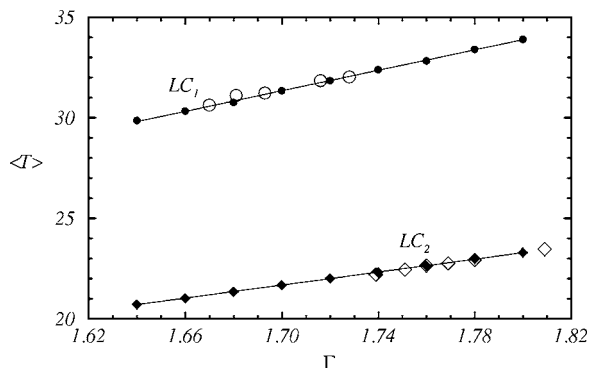


FIG. 6. Variation with Γ of the nondimensional period averaged over Re , $\langle T \rangle$ for LC_1 and LC_2 ; the open symbols are experimentally measured, the filled symbols are numerically computed, and the lines are best fits to the computed data.

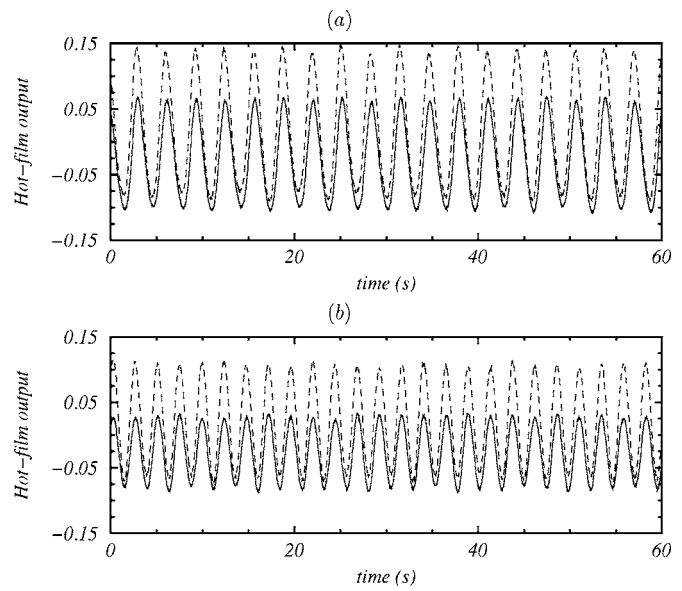


FIG. 7. Hot-film data (time series over 1 min) from the two hot films placed 180° apart on the stationary end plate, showing (a) an LC_1 state at $Re = 2760$ and $\Gamma = 1.704$, and (b) an LC_2 state at $Re = 2750$ and $\Gamma = 1.780$ (each state is asymptotically stable).

Hopf curves, the respective limit cycles become unstable before their amplitudes vanish, and so good extrapolations were not obtained. However, the loci of (Γ, Re) at which they become unstable gives good estimates of the Neimark-Sacker curves NS_1 and NS_2 . In the coexistence region between NS_1 and NS_2 , there is also a quasiperiodic mixed mode, but in this problem it is unstable and so we only observe it indirectly in the early transients of flow evolutions. Above the Hopf curves, all initial conditions eventually evolve to either LC_1 or LC_2 . This is a characteristic signature of a “type I simple” double Hopf bifurcation (using the nomenclature of Ref. 19), and provides a very clear test for experimental evidence of such a bifurcation.

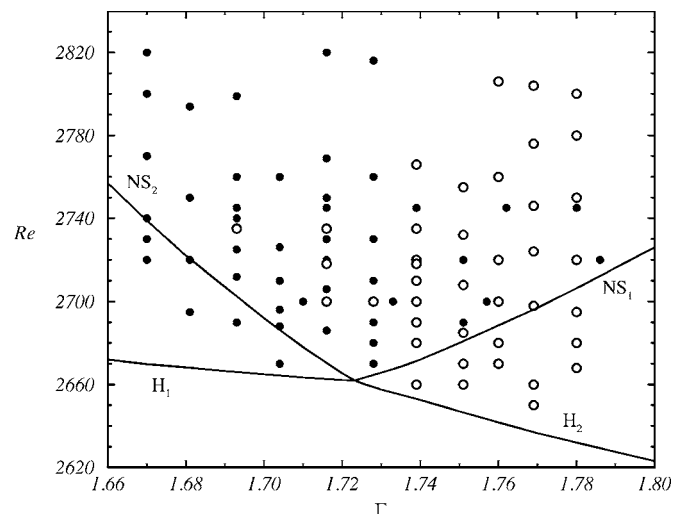


FIG. 8. State diagram showing the numerically determined bifurcation curves H_1 , H_2 , NS_1 , and NS_2 , and loci of experimentally observed stable limit cycles LC_1 (filled symbols) and LC_2 (hollow symbols).

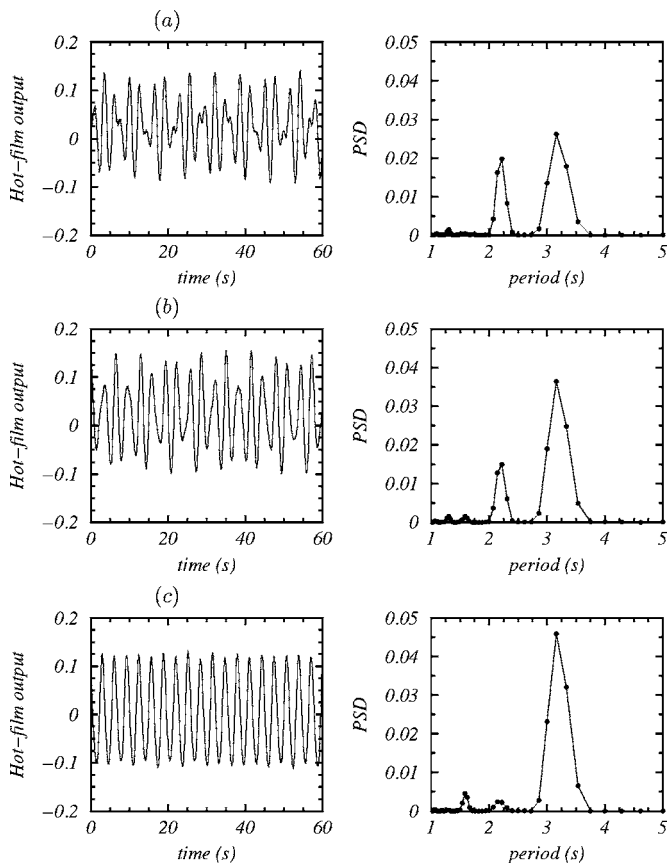


FIG. 9. Hot-film data (time series over 1 min and corresponding power spectral density) taken (a) 4 min, (b) 7 min, and (c) 14 min after startup from rest with $Re=2760$ and $\Gamma=1.704$, showing evolution to an LC_1 state.

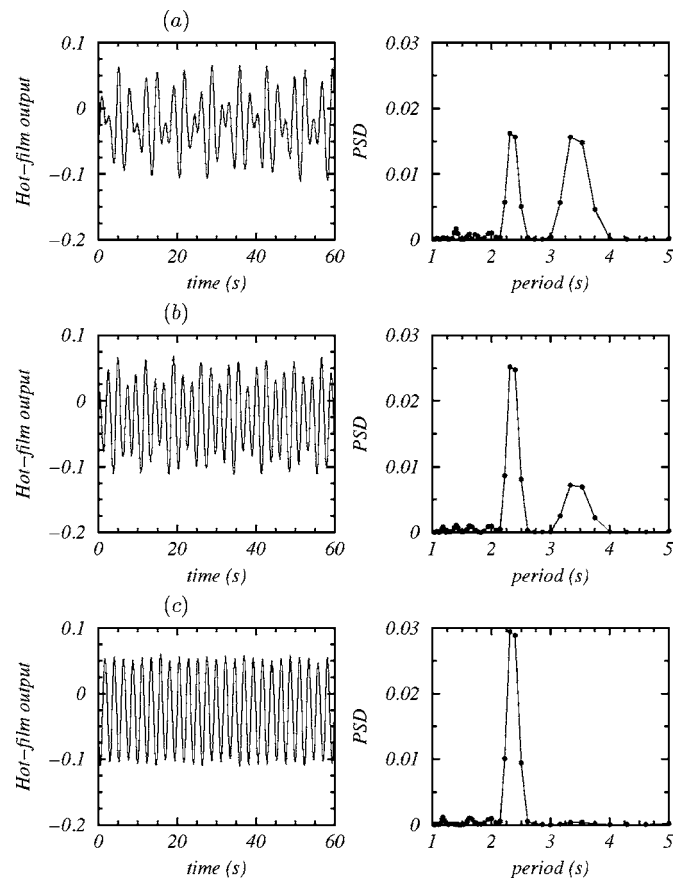


FIG. 10. Hot-film data (time series over 1 min and corresponding power spectral density) taken (a) 9 min, (b) 12 min, and (c) 18 min after startup from rest with $Re=2806$ and $\Gamma=1.76$, showing evolution to an LC_2 state.

V. DETAILS OF THE EXPERIMENTAL MEASUREMENTS

Before presenting the results here, it is important to reiterate that the hot-films used in the present study were not calibrated. Nevertheless, the range of Re (and therefore, velocity) covered in the present study is quite small (less than 5%). Within this small range of velocity variation, the temporal variation in the hot-film signal is approximately proportional to the temporal variation in velocity.

To establish the characteristics of the double Hopf bifurcation and the associated Neimark-Sacker bifurcations, we adopted the same strategy as in the numerical work of Ref. 17, where once a desired state was obtained at a particular point in (Γ, Re) parameter space, a quasistatic parameter sweep was carried out either by fixing Γ and varying Re or vice versa. Fixing Γ and varying Re allowed us to estimate the critical Re for the Hopf bifurcations at particular values of Γ , and by fixing Re and varying Γ , we estimated the Neimark-Sacker bifurcations.

A. Fixed Γ and variable Re

The procedure adopted for this part of the experiment is as follows: For a given Γ , the rotation speed of the disk was started impulsively from rest to a speed corresponding to a

predetermined Reynolds number. Upon reaching the preset condition, the flow was allowed to stabilize over a period of time, usually more than two viscous times (a viscous time unit corresponds to R^2/ν , which is about 250 s, depending on the temperature and glycerin/water ratio). Once the hot-film signal remained unchanged for more than 1 min, the flow was presumed to have reached an asymptotic state, and the hot-film signal was then sampled by a PC for subsequent analysis. Next, a parameter sweep was made along constant Γ by reducing Re (the rotation speed of the disk) very slowly, but stopped at each predetermined Re to obtain the required hot-film measurements in a similar manner as discussed above, until the vicinity of the Hopf bifurcation was reached. Figure 9 shows the temporal evolution to an LC_1 state when the rotating disk was impulsively starting from rest at $\Gamma=1.704$. The left column of the figure is the time series of hot-film output, and the right column is the corresponding power spectral density. At early stages of the flow development (4 min ≈ 0.86 viscous time units), the hot-film signal is quasiperiodic with two dominant frequencies 0.31 and 0.46 Hz, corresponding to the nondimensional periods (scaled by Ω) $T_1 \approx 31.9$ for LC_1 and $T_2 \approx 21.5$ for LC_2 . With increasing time, the LC_1 mode becomes progressively more dominant, until about 16 min after start-up (3.44 viscous time units) when LC_1 prevailed. Starting from rest at another nearby point in parameter space, $\Gamma=1.76$ and

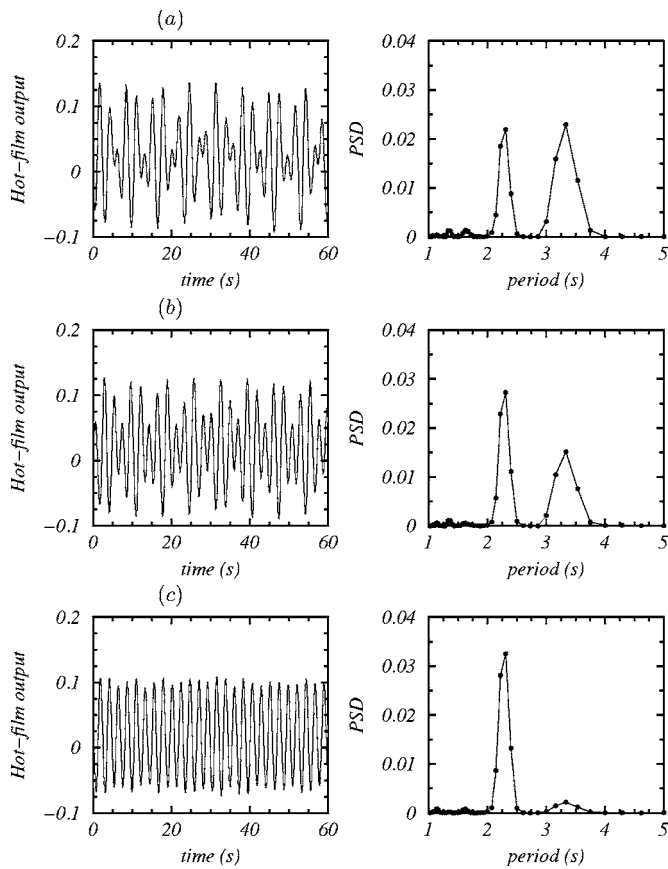


FIG. 11. Hot-film data (time series over 1 min and corresponding power spectral density) showing evolution to an LC_2 state at $\Gamma=1.733$, taken (a) 17 min, (b) 23 min, and (c) 32 min after an impulsive start from rest to $Re=2750$.

$Re=2806$ (see Fig. 10), the initial evolution again has a quasiperiodic character typical of the competition between the two limit cycles, but in this case LC_2 eventually wins.

B. Coexistence of the two limit cycles LC_1 and LC_2

In this part of the investigation, Γ was kept constant and measurements were taken at different Re . For $\Gamma \geq 1.739$, it is found that LC_2 can be obtained by impulsively starting the rotating disk from rest, and likewise for $\Gamma \leq 1.728$, LC_1 can be obtained in the same manner. Depending on initial conditions, it is found that both LC_1 and LC_2 can be obtained at the same Γ and Re . Figures 11 and 12 show this very clearly for $\Gamma=1.733$, where the first figure shows the evolution to LC_2 following an impulsive start of the bottom rotating disk from rest to a predetermined speed (corresponding to $Re=2750$), and the second figure shows how LC_1 was generated, also from rest, but with a gradual increase in Re from 0 to 2750 at the rate $\partial Re/\partial t=5/s$. This is just one of many experimental observations we have made of the coexistence of the two limit cycles LC_1 and LC_2 at the same point in parameter space (Γ, Re) ; which one dominates depends on initial conditions. The coexistence region is in between the two Neimark-Sacker curves NS_1 and NS_2 (see Fig. 8).

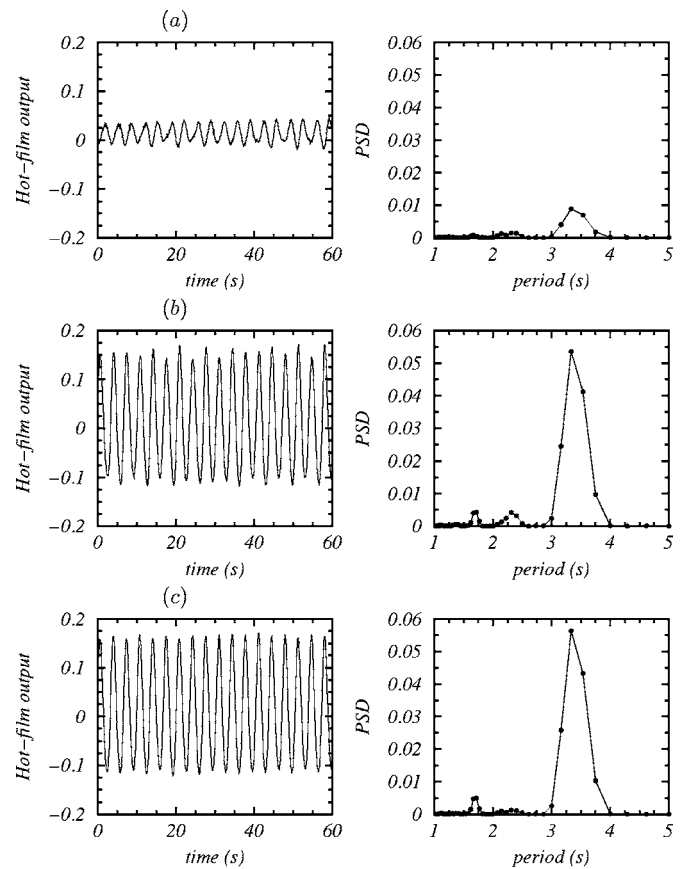


FIG. 12. Hot-film data (time series over 1 min and corresponding power spectral density) showing evolution to an LC_1 state at $\Gamma=1.733$, taken (a) 10 min, (b) 20 min, and (c) 25 min following a gradual start from rest to $Re=2750$ at a rate of $\partial Re/\partial t=5/s$.

C. Determination of critical Reynolds numbers for the Hopf bifurcations

With Γ fixed, reducing Re toward the Hopf bifurcation curve led to a reduction in the amplitude of the hot-film signal (or velocity variation) as the flow approached the steady state. This behavior can be clearly seen in Fig. 13(a) for an LC_2 mode at $\Gamma=1.769$. The critical Reynolds number is then determined by extrapolating to zero the peak-to-peak amplitude of the hot-film. Figure 13(b) shows such an extrapolation from the data in Fig. 13(a), giving an estimated $Re_c \approx 2647$ for LC_2 at $\Gamma=1.769$. Using this procedure, the critical Reynolds numbers for other aspect ratios were also obtained to estimate the Hopf bifurcations H_1 for the onset of LC_1 and H_2 for the onset of LC_2 ; their loci in (Γ, Re) parameter space is presented in Fig. 14 as filled and hollow circles, respectively. The figure also shows the computed H_1 and H_2 curves; the experimental measurements of the critical Re for the Hopf bifurcations at the various Γ are within 2% of the computed values.

D. Fixed Re and variable Γ

The purpose of this part of the investigation is to further verify the coexistence of the two limit cycles LC_1 and LC_2 in (Γ, Re) parametric space, and how these limit cycles transition from one mode to the other when the Neimark-Sacker

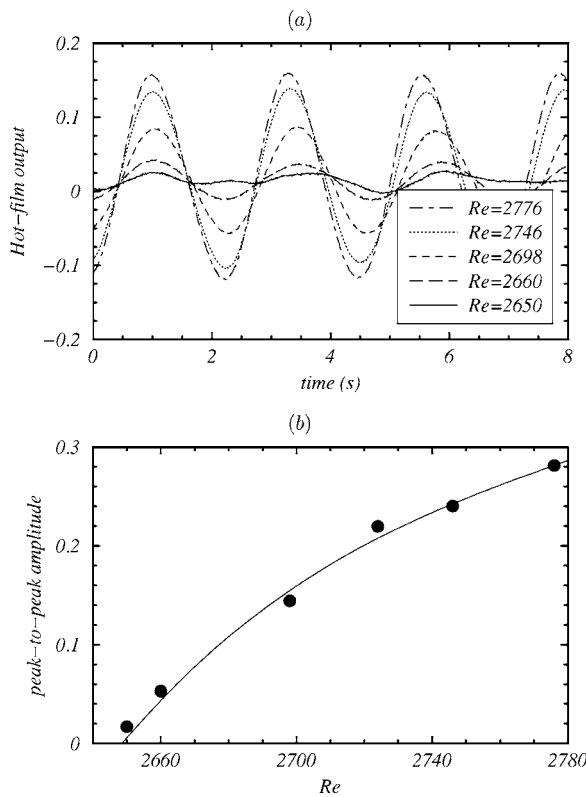


FIG. 13. (a) Hot-film outputs over 8 s, taken once flow transients had died down, of the LC_2 state at $\Gamma=1.769$ for various Re as indicated, (b) variation with Re of the peak-to-peak amplitudes of the time series shown in (a).

curves are crossed. Here, Re was kept constant while Γ was varied. In Fig. 14, the “ \times ” symbols represent LC_2 states that resulted from continuing the LC_1 state past the NS_1 curve following a quasistatic increase in Γ . Likewise, the “+” symbols in the figure represent LC_1 states that resulted from

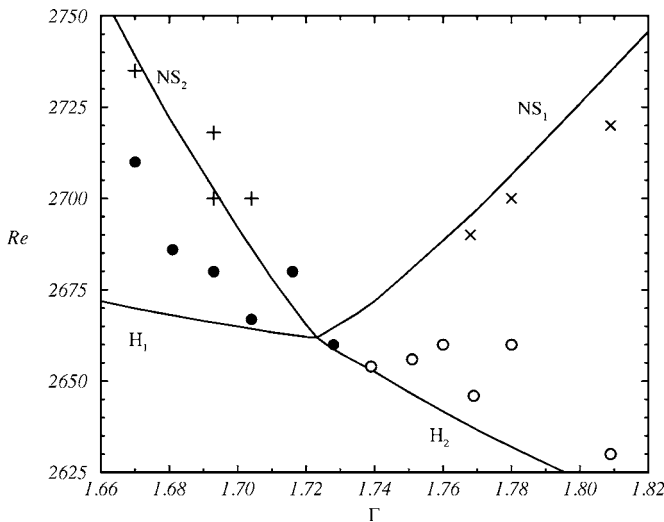


FIG. 14. The curves H_1 , H_2 , NS_1 , and NS_2 are the numerically determined Hopf and Neimark-Sacker bifurcation curves. The filled and hollow circles are experimental estimates of the Hopf bifurcations H_1 and H_2 , determined by fixing Γ , measuring the amplitude of the oscillation at various Re and extrapolating in Re to zero amplitude. The symbols + are experimentally observed LC_1 states that evolved from an LC_2 initial condition on crossing the Neimark-Sacker curve NS_2 as Γ was quasistatically reduced, and the symbols \times are experimentally observed LC_2 states that evolved from an LC_1 initial condition on crossing the Neimark-Sacker curve NS_1 as Γ was quasistatically increased.

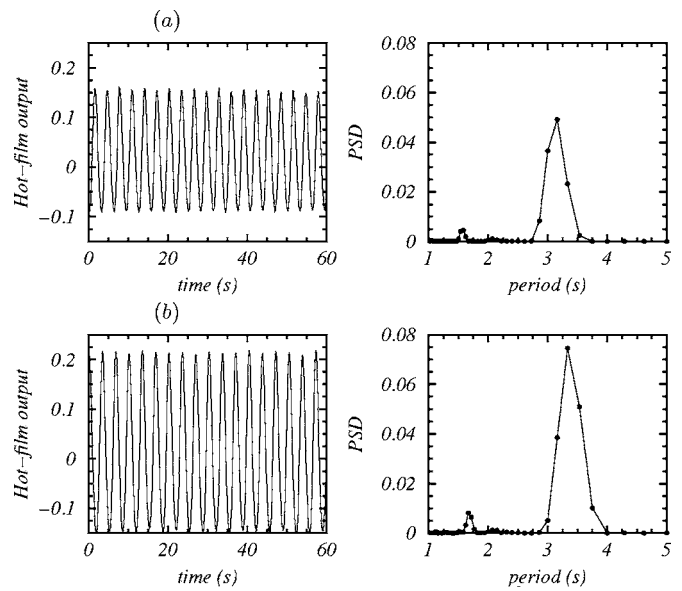


FIG. 15. Hot-film data (time series over 1 min and corresponding power spectral density) taken after transients have died down (more than two viscous time units), showing an LC_1 state at $Re=2750$ and (a) $\Gamma=1.693$ and (b) $\Gamma=1.780$.

continuing the LC_2 state past the NS_2 curve following a quasistatic decrease in Γ . These events lie very close to the numerically determined Neimark-Sacker bifurcation curves, as shown in the figure.

Starting from $\Gamma=1.693$ at $Re=2745$, LC_1 was the mode that emerged following an impulsive start from rest. By then increasing Γ in quasisteady increments from $\Gamma=1.716$ to 1.739 to 1.762 to 1.78, the LC_1 flow state was maintained indefinitely. Typical hot-film results presented in Fig. 15 show that the LC_1 mode remains stable up to $\Gamma=1.78$. This is consistent with our numerical computations. We repeated

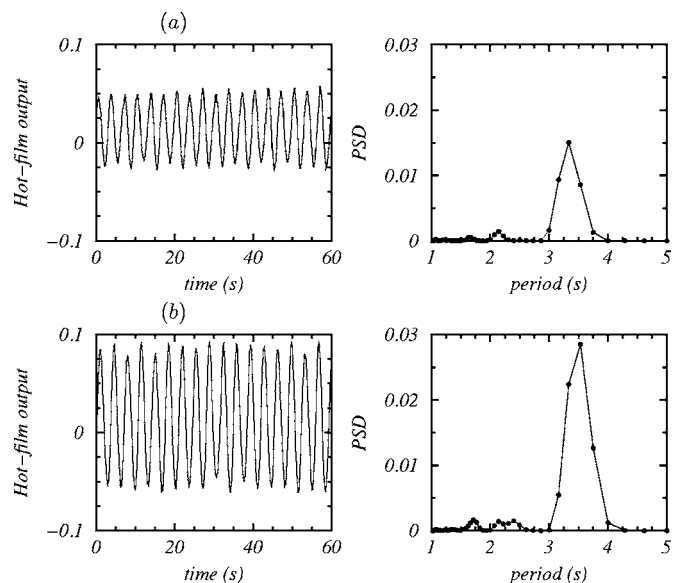


FIG. 16. Hot-film data (time series over 1 min and corresponding power spectral density) taken after transients have died down (more than two viscous time units), showing an LC_1 state at $Re=2700$ and (a) $\Gamma=1.716$ and (b) $\Gamma=1.757$.

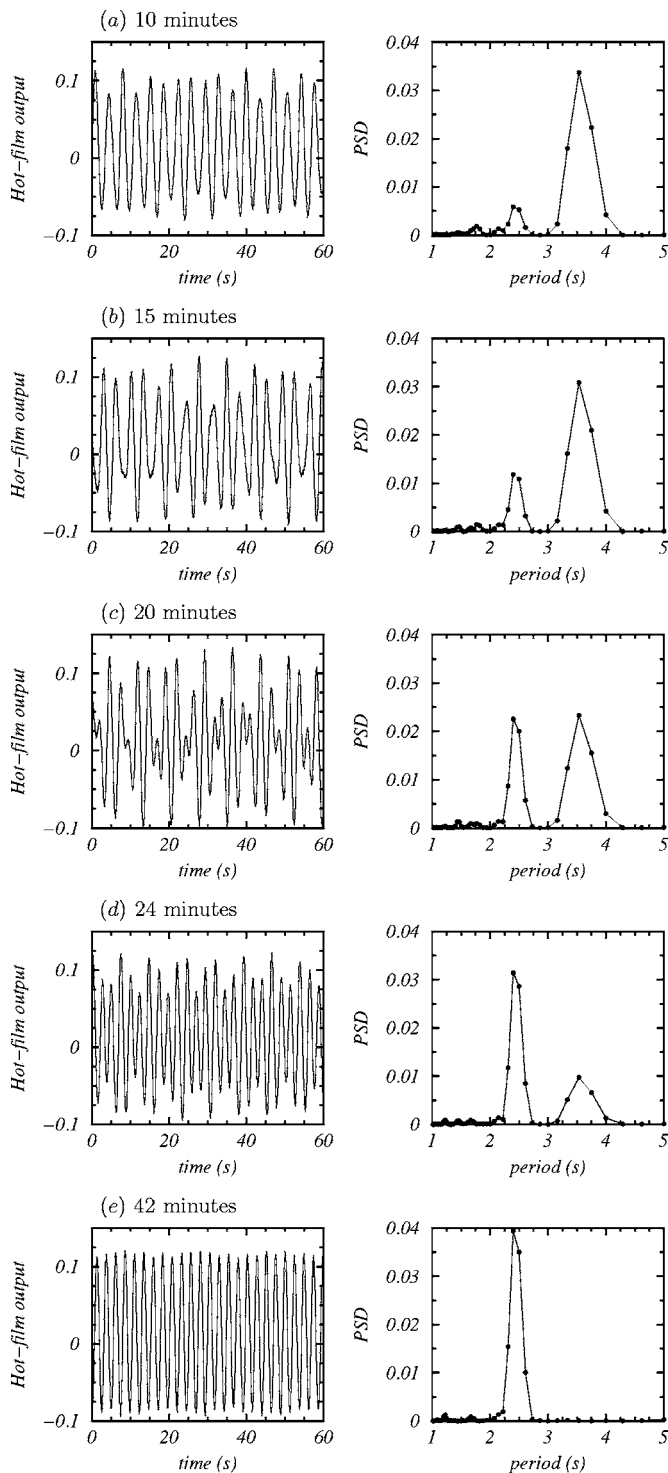


FIG. 17. Hot-film data (time series over 1 min and corresponding power spectral density) taken at times as indicated, starting with an LC_1 state at $Re=2700$ and $\Gamma=1.757$ and increased to $\Gamma=1.780$.

this procedure at lower $Re=2700$, starting at $\Gamma=1.716$, where the flow evolved to LC_1 following an impulsive start from rest. As Γ was varied in small discrete steps, LC_1 was maintained up to 1.757, as shown in Fig. 16. However, when Γ was increased from 1.757 to 1.78, LC_1 lost stability and transitioned to LC_2 after a long transient during which energy was transferred from oscillations with the period of LC_1 to oscillations with the period of LC_2 . Figure 17 shows the

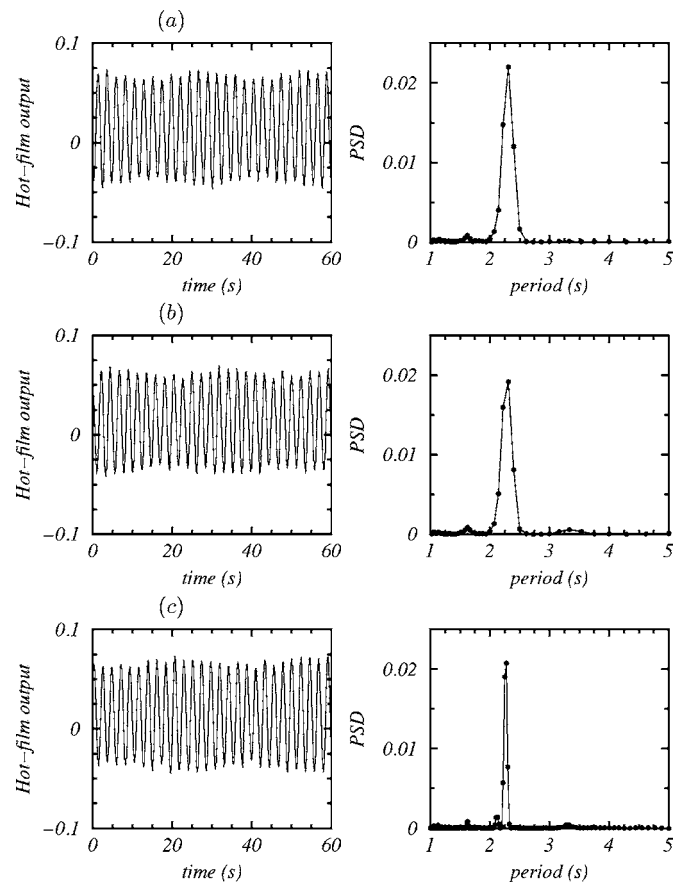


FIG. 18. Hot-film data (time series over 1 min and corresponding power spectral density) taken after transients have died down (more than two viscous time units), showing LC_2 states at $Re=2700$ and (a) $\Gamma=1.739$, (b) $\Gamma=1.728$, and (c) $\Gamma=1.716$; the initial condition at a given Γ was the LC_2 state at the next largest Γ value.

corresponding hot-film output. At early stages of the flow evolution (within the first 10 min), LC_1 was still dominant, but with noticeable irregularity in the time series from the hot-film output. After 15 min, the irregularity became stronger signaling the nonlinear saturation of LC_2 . At a time of 20 min, the energy in the two modes is comparable, and by 42 min, all the energy is in mode LC_2 .

The transition from LC_2 to LC_1 across the Neimark-Sacker curve NS_2 follows a process similar to the transition from LC_1 to LC_2 on crossing the Neimark-Sacker curve NS_1 described above, and the results are presented in Figs. 18 and 19. At $\Gamma=1.739$ and $Re=2700$, LC_2 was the dominant mode, but as Γ was reduced gradually, the hot-film output time series became modulated and irregular, leading to the eventual dominance of LC_1 . This was repeated at many other Re in order to estimate the two Neimark-Sacker bifurcations at various Re , and the results are presented in Fig. 14. Though the experimental bifurcation locations are slightly shifted with respect to the computed curves, the shift is very small (about 2%, which is well within experimental uncertainty). The experimental results clearly reveal the characteristics of the double Hopf bifurcation under laboratory conditions.

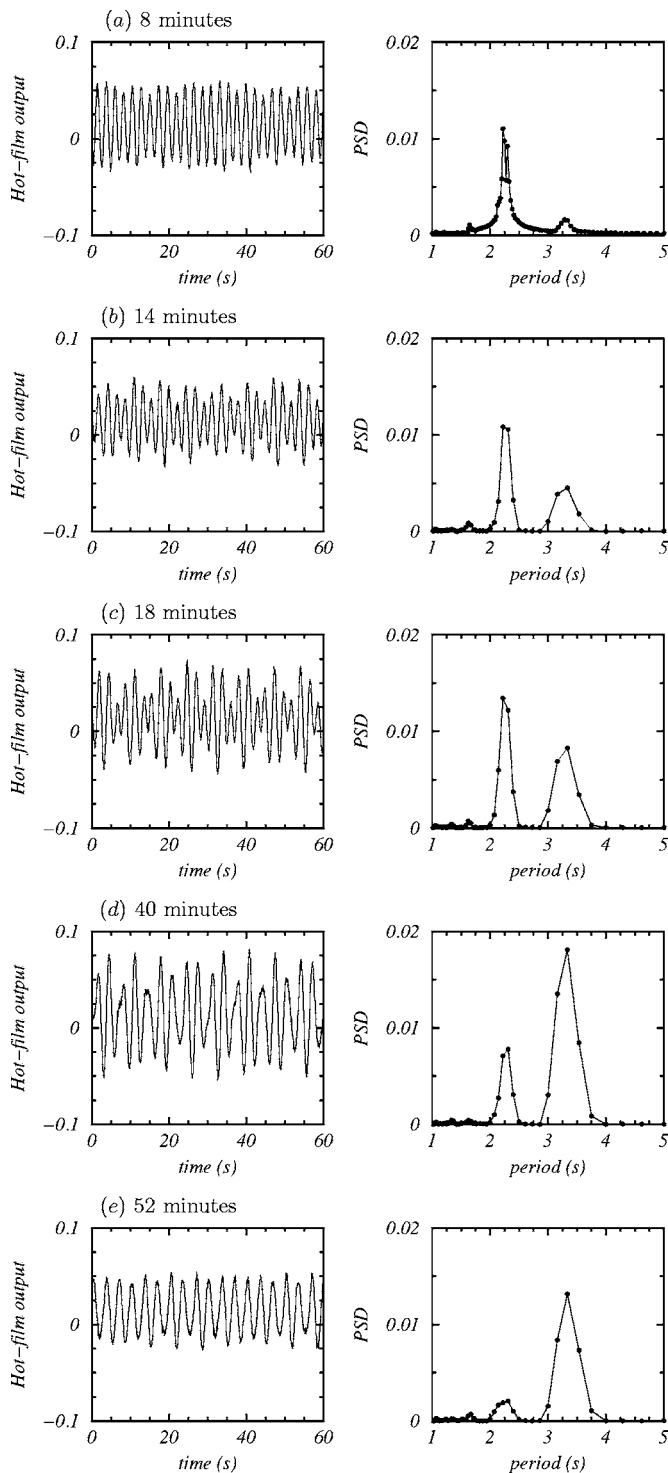


FIG. 19. Hot-film data (time series over 1 min and corresponding power spectral density) taken at times as indicated, starting with an LC_2 state at $Re=2700$ and $\Gamma=1.716$ and decreased to $\Gamma=1.704$.

VI. DISCUSSION AND CONCLUSIONS

Using linear stability analysis, Ref. 7 showed the existence of an axisymmetric double Hopf bifurcation. Our hot-film measurements provide, for the first time, experimental evidence of the existence of this double Hopf bifurcation, and reveal the presence of two stable coexisting axisymmetric limit cycles with periods of approximately 31 and 22 and

mode competition between them. These results are also captured in our nonlinear computations, which clearly identify the double Hopf bifurcation as “type I simple” (using the nomenclature of Ref. 19), with the characteristic signatures that the two Hopf bifurcations are supercritical and that there is a wedge-shaped region in parameter space where both limit cycles are stable, delimited by Neimark-Sacker bifurcation curves. Despite numerous warnings that the enclosed swirling flow is extremely sensitive to small imperfections,^{10,20} our experimental results show that if the imperfections are sufficiently small (we make no attempt here to rigorously quantify “small” in the experimental setting, but others^{10,20} have done so numerically for very specific types of imperfections), the qualitative dynamics do not change and, at least for this problem, the quantitative effects are a very small shift in the location of the bifurcation curves.

While linear stability predicts the double Hopf bifurcation, it says nothing about the nonlinear behavior of the flow following the bifurcation. In particular, the linear stability analysis of the steady axisymmetric basic state does not provide information on the Neimark-Sacker bifurcations NS_1 and NS_2 (which are Hopf-type instabilities of the limit cycle states); the loci of these bifurcations delineate the region of mode competition between the two limit cycles. In order to say anything about this competition, one must do some nonlinear analysis. The simplest thing to do is to perform a center manifold reduction and a normal form analysis in the neighborhood of the double Hopf bifurcation.^{11,21} Doing such an analysis gives a multitude of possible nonlinear scenarios describing all possible competition dynamics.¹⁹ In order to pinpoint which scenario corresponds to a particular flow problem requires detailed spatio-temporal information about the bifurcating limit cycles, which may be obtained from quantitative experimental measurements or fully nonlinear computations. We have obtained both in this study, and they both give consistent results indicating that the double Hopf bifurcation is “type I simple.” Further, our experiment and fully nonlinear investigation reveals that the dynamics associated with the center manifold reduction persist over a large range of Re and Γ , as illustrated in Fig. 8. Furthermore, these dynamics are robust to the low-level imperfections and noise that are inherently present in the physical laboratory experiment.

ACKNOWLEDGMENTS

J.M.L. gratefully acknowledges the support from the National Science Foundation (Grant No. DMS-0505489), and the hospitality of the Department of Mechanical Engineering, National University of Singapore for part of the time during which this work was performed.

¹M. P. Escudier, “Observations of the flow produced in a cylindrical container by a rotating endwall,” *Exp. Fluids* **2**, 189 (1984).

²H. J. Lugt and M. Abboud, “Axisymmetric vortex breakdown with and without temperature effects in a container with a rotating lid,” *J. Fluid Mech.* **179**, 179 (1987).

³J. M. Lopez, “Axisymmetric vortex breakdown: Part 1. Confined swirling flow,” *J. Fluid Mech.* **221**, 533 (1990).

⁴J. M. Lopez and A. D. Perry, “Axisymmetric vortex breakdown: Part 3.

- Onset of periodic flow and chaotic advection," J. Fluid Mech. **234**, 449 (1992).
- ⁵J. N. Sorensen and E. A. Christensen, "Direct numerical simulation of rotating fluid flow in a closed cylinder," Phys. Fluids **7**, 764 (1995).
- ⁶J. M. Lopez, F. Marques, and J. Sanchez, "Oscillatory modes in an enclosed swirling flow," J. Fluid Mech. **439**, 109 (2001).
- ⁷A. Y. Gelfgat, P. Z. Bar-Yoseph, and A. Solan, "Three-dimensional instability of axisymmetric flow in a rotating lid-cylinder enclosure," J. Fluid Mech. **438**, 363 (2001).
- ⁸A. Spohn, M. Mory, and E. J. Hopfinger, "Experiments on vortex breakdown in a confined flow generated by a rotating disk," J. Fluid Mech. **370**, 73 (1998).
- ⁹F. Sotiropoulos, D. R. Webster, and T. C. Lackey, "Experiments on Lagrangian transport in steady vortex-breakdown bubbles in a confined swirling flow," J. Fluid Mech. **466**, 215 (2002).
- ¹⁰M. C. Thompson and K. Hourigan, "The sensitivity of steady vortex breakdown bubbles in confined cylinder flows to rotating lid misalignment," J. Fluid Mech. **496**, 129 (2003).
- ¹¹J. Guckenheimer and P. Holmes, *Nonlinear Oscillations, Dynamical Systems, and Bifurcations of Vector Fields* (Springer, New York, 1983).
- ¹²P. Holmes, "Some remarks on chaotic particle paths in time-periodic, three-dimensional swirling flows," Contemp. Math. **28**, 393 (1984).
- ¹³A. Y. Gelfgat, "Three-dimensionality of trajectories of experimental tracers in a steady axisymmetric swirling flow: Effect of density mismatch," Theor. Comput. Fluid Dyn. **16**, 29 (2002).
- ¹⁴J. M. Lopez and A. D. Perry, "Periodic axisymmetric vortex breakdown in a cylinder with a rotating end wall," Phys. Fluids A **4**, 1871 (1992).
- ¹⁵J. M. Lopez, F. Marques, and J. Shen, "An efficient spectral-projection method for the Navier-Stokes equations in cylindrical geometries. II. Three dimensional cases," J. Comput. Phys. **176**, 384 (2002).
- ¹⁶F. Marques and J. M. Lopez, "Precessing vortex breakdown mode in an enclosed cylinder flow," Phys. Fluids **13**, 1679 (2001).
- ¹⁷F. Marques, J. M. Lopez, and J. Shen, "Mode interactions in an enclosed swirling flow: A double Hopf bifurcation between azimuthal wavenumbers 0 and 2," J. Fluid Mech. **455**, 263 (2002).
- ¹⁸J. M. Lopez, "Rotating and modulated rotating waves in transitions of an enclosed swirling flow," J. Fluid Mech. **553**, 323 (2006).
- ¹⁹Y. A. Kuznetsov, *Elements of Applied Bifurcation Theory*, 2nd ed. (Springer, New York, 1998).
- ²⁰Y. Ventikos, "The effect of imperfections on the emergence of three-dimensionality in stationary vortex breakdown bubbles," Phys. Fluids **14**, 13 (2002).
- ²¹J. E. Marsden and M. McCracken, *The Hopf Bifurcation and Its Applications*, Appl. Math. Sci. Vol. 19 (Springer, New York, 1976).